Lipophilic siRNA targets albumin in situ and promotes bioavailability, tumor penetration, and carrier-free gene silencing

Samantha M. Sarett[a], Thomas A. Werfel[a], Linus Lee[a], Meredith A. Jackson[a], Kameron V. Kilchrist[a], Dana Brantley-Sieders[b], and Craig L. Duvall[a,1]

[a]Department of Biomedical Engineering, Vanderbilt University, Nashville, TN 37235; and [b]Department of Medicine, Vanderbilt University Medical Center, Nashville, TN 37232

Clinical translation of therapies based on small interfering RNA (siRNA) is hampered by siRNA's comprehensively poor pharmacokinetic properties, which necessitate molecule modifications and complex delivery strategies. We sought an alternative approach to commonly used nanoparticle carriers by leveraging the long-lived endogenous serum protein albumin as an siRNA carrier. We synthesized siRNA conjugated to a diacyl lipid moiety (siRNA-L_2), which rapidly binds albumin in situ. siRNA-L_2, in comparison with unmodified siRNA, exhibited a 5.7-fold increase in circulation half-life, an 8.6-fold increase in bioavailability, and reduced renal accumulation. Benchmarked against leading commercial siRNA nanocarrier in vivo jetPEI, siRNA-L_2 achieved 19-fold greater tumor accumulation and 46-fold increase in per-tumor-cell uptake in a mouse orthotopic model of human triple-negative breast cancer. siRNA-L_2 penetrated tumor tissue rapidly and homogeneously; 30 min after i.v. injection, siRNA-L_2 achieved uptake in 99% of tumor cells, compared with 60% for jetPEI. Remarkably, siRNA-L_2 achieved a tumor:liver accumulation ratio >40:1 vs. <3:1 for jetPEI. The improved pharmacokinetic properties of siRNA-L_2 facilitated significant tumor gene silencing for 7 d after two i.v. doses. Proof-of-concept was extended to a patient-derived xenograft model, in which jetPEI tumor accumulation was reduced fourfold relative to the same formulation in the orthotopic model. The siRNA-L_2 tumor accumulation diminished only twofold, suggesting that the superior tumor distribution of the conjugate over nanoparticles will be accentuated in clinical situations. These data reveal the immense promise of in situ albumin targeting for development of translational, carrier-free RNAi-based cancer therapies.

siRNA delivery | RNAi | albumin binding | pharmacokinetics | tumor delivery

Harnessing the therapeutic potential of small interfering RNA (siRNA) hinges upon enhancing its pharmacokinetic properties to overcome in vivo delivery barriers. Unmodified siRNA exhibits rapid renal clearance from circulation, leading to removal through the urine (1) and allowing minimal bioavailability in target tissues. Improving delivery of siRNA via encapsulation in nanoparticulate carrier systems has been the principal strategy used by the field. Nanocarriers can improve circulation half-life, resistance to degradation, intracellular uptake, and ultimately gene silencing potency (2–5). However, commonly used cationic lipid/polymer formulations are complex and expensive to synthesize and can be toxic and/or immunogenic (6, 7). Additionally, their preferential uptake by clearance organs such as the liver and spleen hinders delivery to target tissues (4, 8). siRNA conjugates have emerged as an alternative to nanocarrier-mediated delivery (9–14), offering the possibility of improving siRNA pharmacokinetics without requiring a more complex delivery vehicle. Alnylam Pharmaceuticals has demonstrated high gene silencing potency of a trivalent N-Acetylgalactosamine (GalNAc) siRNA conjugate, which binds with high specificity and affinity to the asialoglycoprotein receptor on hepatocytes (15, 16).

Carrier-free gene silencing has also been achieved in the liver with siRNA–cholesterol conjugates (1, 14), but the development of siRNA conjugates that efficiently deliver to nonhepatic tissues is an unmet need. Here, we developed an siRNA conjugate that leverages endogenous albumin as a chaperone. We anticipate that albumin-associated siRNA will show particular promise as a cancer therapeutic by extending the circulation time of siRNA, enabling efficient tumor tissue penetration, and leveraging the propensity of tumor cells to internalize albumin (17, 18).

The enhanced permeability and retention (EPR) effect, based upon the high vascular permeability and diminished lymphatic drainage at tumor sites, suggests a preferential tumor accumulation of particles of nanocarrier size (~100 nm). However, the EPR phenomenon as a tumor targeting strategy has recently come under intense scrutiny due to the discrepancy observed between preclinical and clinical efficacy of nanoparticle-based cancer therapeutics (19–22). There is a growing appreciation that among wildly heterogeneous human cancers, the EPR effect may be only relevant in select tumor or patient subsets. In particular, the widespread "leakiness" of tumor vasculature, a characteristic of rapidly developing mouse tumor models, has likely been exaggerated in its relevance to slower-forming human lesions (23). The field of nanomedicine has responded to these realizations with efforts to

Significance

Small interfering RNA (siRNA) has the capacity to silence traditionally undruggable targets, but in vivo delivery barriers limit clinical translation of siRNA, especially for nonhepatic targets such as solid tumors. Most delivery strategies for RNAi cancer therapies focus on synthetic nanocarriers, but their shortcomings include limited delivery to and variable distribution throughout the target site and low therapeutic indices due to nonspecific, carrier-associated toxicities. A diacyl lipid-modified siRNA can leverage albumin as an endogenous carrier, resulting in comprehensively enhanced pharmacokinetic properties that translate to greater quantity and homogeneity of tumor accumulation relative to nanocarriers. The albumin-binding siRNA conjugate strategy is synthetically simple and safe at high doses, and thus is a translatable and potentially transformative option for RNAi oncology therapies.

enhance understanding of nanoparticle performance in animal models (24–27), strategies to normalize tumor vasculature (28), systematic investigations into ideal nanoparticle characteristics (24, 29), and a focus on smaller (20–30-nm-sized) nanocarriers (24, 30, 31). Despite the promise of these approaches, the diversity of human cancers necessitates equivalently diverse delivery approaches (23, 32) and opportunity for improvement remains, particularly in the area of enhancing uniformity of tumor distribution. Nanoparticles typically exhibit concentration of dose near leaky vessels but not within more avascular tumor regions (33, 34), resulting in inhomogeneous efficacy and higher potential for incomplete remission and recurrence. Smaller, long-circulating siRNA conjugates may offer an alternative that creates more homogeneous therapeutic distribution within tumors. Indeed, the apparent tissue permeability of the serum protein albumin [hydrodynamic size ~7.2 nm (35)] is consistently more than fourfold greater than that of 100-nm liposomes in a variety of mouse models of breast cancer (36). Here, we sought to design an siRNA conjugate that "hitchhikes" on long-circulating albumin to confer siRNA molecules with an unprecedented combination of circulation persistence and high tissue penetration to enable systemic, carrier-free delivery of siRNA for oncological applications.

In situ targeting of albumin following i.v. delivery is a viable strategy because endogenous albumin is the most abundant serum protein (>40 mg/mL) and has a circulation half-life of about 20 d (37). It is also a natural carrier of and has a high affinity for poorly soluble lipids (35, 37). Albumin has been investigated extensively as a carrier and a conjugate for small molecules as well as protein therapeutics; albumin-based therapeutics like Abraxane, Levemir, and Optison have achieved clinical relevance (35, 38), demonstrating the translatability of this approach. Previous work has established the utility of interaction of high- and low-density lipoproteins with cholesterol-conjugated siRNA (14, 39–42), but the natural trafficking of these lipoproteins concentrates the therapy in the hepatocytes of the liver. The potential of albumin-bound siRNA has been minimally explored (42, 43). In our unique strategy, we exploit the capacity of albumin to bind fatty acids by modifying siRNA with a lipidic moiety designed for high-affinity albumin binding. Previously, this hydrophobic modification for in situ albumin targeting was used to promote delivery of CpG DNA to lymph nodes for vaccine applications (44). We pursued modification of siRNA with a lipidic albumin-targeting agent rather than alternative albumin-binding molecules like peptide domains (45) and a truncated Evans blue molecule (46) because hydrophobically modified siRNA exhibits improved resistance to nucleases and enhanced cellular internalization (10). Thus, the strategic choice of modification with an albumin-binding lipid has the potential to confer additional advantages in siRNA stability and cell membrane interactions for uptake and endosomal escape in addition to circulation persistence, tissue penetration, and biodistribution. To investigate the clinical potential of our siRNA conjugate, we examined its efficacy as a systemic RNAi cancer therapeutic by evaluating delivery and gene silencing in translationally relevant models of human triple-negative breast cancer.

Results

Purified siRNA-L$_2$ Conjugate Binds to Albumin. To synthesize siRNA conjugated to a diacyl lipid moiety (siRNA-L$_2$), a single-stranded amine-modified siRNA was reacted with an NHS ester/dibenzocyclooctyne heterobifunctional cross-linker and subsequently conjugated with 1,2-distearoyl-sn-glycero-3-phosphoethanolamine-N-[azido(polyethylene glycol)-2000] (DSPE-PEG$_{2000}$-azide) to generate siRNA-L$_2$ (Fig. 1A and *SI Appendix*, Fig. S1A). The fully purified L$_2$ conjugates were obtained by reverse-phase chromatography and purity was confirmed by mass spectrometry (Fig. 1B and *SI Appendix*, Fig. S1B). Following purification, sense strand siRNA-L$_2$ was annealed to the corresponding antisense strand (for imaging
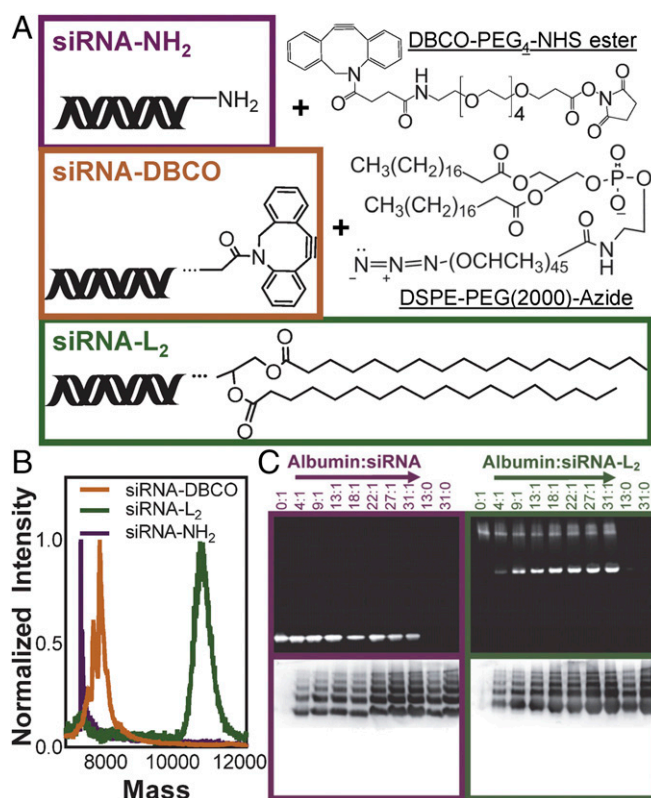

Fig. 1. Successfully synthesized and purified siRNA-L$_2$ conjugate binds to albumin. (A) Abbreviated structures of reactants and final oligonucleotide-L$_2$ conjugate. (B) MALDI-TOF mass spectrometry of the original amine-modified siRNA, the DBCO intermediate, and the L$_2$ conjugate. (C) Albumin binding measured by gel stained for siRNA (Top) and protein (Bottom). siRNA-L$_2$ migrates as a micellar population alone and comigrates with albumin, whereas unmodified siRNA does not migrate with albumin. Note that albumin shows up as multiple bands due to running in nondenaturing, native gel conditions.

studies, the antisense strand was Cy5-labeled). It was confirmed that conjugation of the L$_2$ moiety to siRNA did not significantly impact its inherent gene silencing activity, as demonstrated by in vitro knockdown evaluation of siRNA and siRNA-L$_2$ delivered via the commercial transfection reagent in vivo jetPEI (*SI Appendix*, Fig. S1C).

The albumin-binding capacity of siRNA-L$_2$ was confirmed using a nondenaturing, native PAGE assay (Fig. 1C and *SI Appendix*, Fig. S2A). siRNA-L$_2$ alone migrates above the albumin band because it exists as a micellar population at the concentration loaded into the gel (0.05 mg/mL), whereas critical micelle concentration is 1.4 μg/mL (*SI Appendix*, Fig. S2B). As the albumin:siRNA-L$_2$ ratio increases, more siRNA-L$_2$ binds to and migrates with albumin. Unmodified siRNA does not bind to albumin to any degree at any of the concentrations tested. Evaluation of siRNA-L$_2$ binding to albumin via isothermal calorimetry further confirmed spontaneous association of the molecules (dissociation constant was 1.38 μM; *SI Appendix*, Fig. S2C). Binding of L$_2$ conjugates to albumin in the presence of complete serum was also evaluated by gel migration assay, revealing preferential binding to the albumin component of serum (*SI Appendix*, Fig. S3A).

Albumin Binding of siRNA-L$_2$ Enhances Circulation Time and Reduces Rapid Renal Clearance. To characterize the in vivo pharmacokinetics of siRNA-L$_2$ in comparison with unmodified siRNA, circulation persistence was evaluated in real time using intravital confocal microscopy following i.v. injection. The circulation
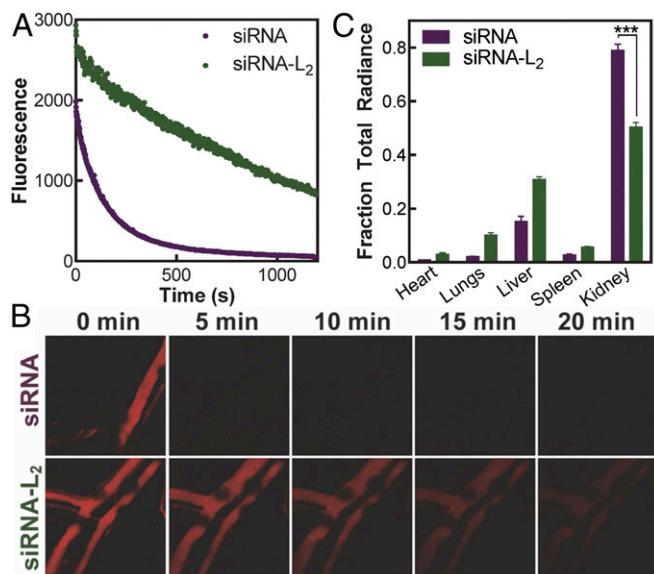
Fig. 2. Conjugation of diacyl lipid to oligonucleotides increases circulation half-life and reduces renal clearance. (*A*) Cy5-labeled siRNA-L$_2$ and siRNA fluorescence in the blood measured in real time intravitally by confocal microscopy after i.v. injection of CD1 mice. (*B*) Representative images of fluorescence in mouse blood vessels over time. (*C*) Organ biodistribution of siRNA and siRNA-L$_2$ at 20 min after i.v. injection. $n = 3$, SE shown; ***$P < 0.001$.

half-life ($t_{1/2}$) of siRNA-L$_2$ was 5.7-fold longer than unmodified siRNA (Fig. 2 *A* and *B* and Table 1). Additionally, the area under the curve, a measure of bioavailability of systemically delivered therapeutics, was 8.6-fold greater for the L$_2$-conjugate compared with unmodified oligonucleotide. To evaluate in situ albumin binding, serum samples from mice injected with siRNA-L$_2$ (blood collection at 20 min postinjection) were evaluated via PAGE gel migration assay and revealed the presence of albumin-bound siRNA-L$_2$ (*SI Appendix*, Fig. S3B). These data confirm that albumin acts as a chaperone for siRNA-L$_2$ in vivo and establish that siRNA-L$_2$ association with albumin confers significant improvements in siRNA pharmacokinetics. To support these studies, the time scale of degradation of unmodified and L$_2$-modified oligonucleotides was investigated. siRNA and siRNA-L$_2$ showed resistance to degradation in serum over the pharmacokinetic time frame assessed, and L$_2$ modification imparted a slight improvement in resistance to serum degradation (*SI Appendix*, Fig. S3 *C* and *D*).

Biodistribution of siRNA vs. siRNA-L$_2$ was evaluated in excised organs at 20 min postinjection. For in vivo studies, siRNA-L$_2$ exhibited increased accumulation in almost all organs, likely due to its prolonged circulation time and reduced clearance into the urine in comparison with unmodified siRNA (Fig. 2C). The kidneys were the sole exception, showing significantly more unmodified siRNA accumulation (a 1.6-fold greater fraction of the total organ radiance) at this early time point. This illustrates that using albumin as a natural carrier for siRNA-L$_2$ reduces acute clearance through the renal route.

siRNA-L$_2$ Outperforms a Leading in Vivo Nanoparticle Carrier in Safety and Tumor Accumulation.

The reduction in kidney accumulation and prolonged circulation half-life of siRNA-L$_2$ motivated a comparison with commercially available in vivo nanoparticles. Of particular interest is the biodistribution profile of siRNA-L$_2$ in comparison with typical nanocarriers, as high uptake by mononuclear phagocytic system organs (the liver and the spleen) can result in minimal dose accumulation at the target site (47). Compared with nanoparticles, siRNA-L$_2$ is expected to avoid

this off-target accumulation and to more readily penetrate tumor tissue.

siRNA-L$_2$ was compared with a leading formulation for nanoparticle-based in vivo nucleic acid delivery, in vivo jetPEI. In vivo jetPEI nanoparticles (jetPEI NPs) have been used in clinical trials, and this comparison is therefore a stringent test for therapeutic potential (48). Before in vivo biodistribution studies, tolerated doses were determined for siRNA-L$_2$ and jetPEI NPs. siRNA-L$_2$ is expected to avoid the toxic side effects associated with high doses of cationic nanocarriers, permitting safe use at higher dosages and potentially expanding the ultimate therapeutic index of siRNA drugs. Toxicity was investigated by monitoring mouse body weight and quantifying blood chemistry markers of liver [alanine aminotransferase (ALT) and aspartate aminotransferase (AST)] and kidney [blood urea nitrogen (BUN) and creatinine] toxicity. Mice injected with an siRNA-L$_2$ dose of 10 mg/kg exhibited normal ALT, AST, and BUN levels statistically equivalent to those of saline-injected mice; these mice also showed no change in body weight (*SI Appendix*, Fig. S4 *A–E*). Delivery of jetPEI NPs at a dose of 1 mg/kg created no signs of toxicity, but doubling that dose to 2 mg/kg resulted in mortality for three of four mice and showed marked hepatic and renal toxicity in the single surviving mouse. These data suggest that siRNA-L$_2$ is a safer alternative to nanocarrier-based delivery with the potential for a much broader therapeutic index. The maximum tolerated dose (MTD) of 1 mg/kg for in vivo jetPEI and a well-tolerated dose of 10 mg/kg for siRNA-L$_2$ were used in subsequent studies (MTD not determined for siRNA-L$_2$).

The biodistribution profile of the L$_2$ conjugate vs. jetPEI NPs was evaluated in a mouse orthotopic xenograft tumor model. siRNA-L$_2$ or jetPEI NPs were injected i.v. into tumor-bearing mice and organs were evaluated for siRNA accumulation. Comparing the absolute radiance in the organs over time from mice treated with jetPEI NPs or siRNA-L$_2$, it is evident that the 10-mg/kg treatment of siRNA-L$_2$ significantly enhances accumulation in all of the organs at an acute (30 min) time point (Fig. 3A and *SI Appendix*, Figs. S5 and S6A). Notably, the vast majority of siRNA-L$_2$ was cleared from all organs excepting the kidneys and tumors by 24 h (Fig. 3A and *SI Appendix*, Fig. S6). jetPEI NPs, in contrast, create higher proportional delivery to and retention within the mononuclear phagocyte system (MPS) clearance organs (the liver and spleen) (Fig. 3B).

The in vivo tolerability of high siRNA-L$_2$ doses enables a remarkable increase in tumor accumulation (Fig. 3 *C* and *D*). The area under the curve within the tumor was 19.3-fold higher for siRNA-L$_2$ at 10 mg/kg than for the maximum tolerated dose of jetPEI NPs (Table 2). Dose-matched siRNA-L$_2$ at 1 mg/kg also outperforms jetPEI NPs in this measure of tumor accumulation by 2.4-fold. Additionally, the fraction of the total organ radiance in the tumors is consistently higher for siRNA-L$_2$ at both doses compared with jetPEI NPs, indicating more preferential tumor accumulation with siRNA-L$_2$ relative to jetPEI NPs.

To further annotate the ability of siRNA-L$_2$ to avoid the typical MPS organ accumulation of nanoparticles and accumulate preferentially within tumors, we evaluated the tumor:liver radiance ratio. At the 10-mg/kg siRNA-L$_2$ dose, a tumor:liver accumulation of more than 40:1 was observed at both 24 and 48 h, indicating

Table 1. Key pharmacokinetics parameters for siRNA-L$_2$ vs. siRNA

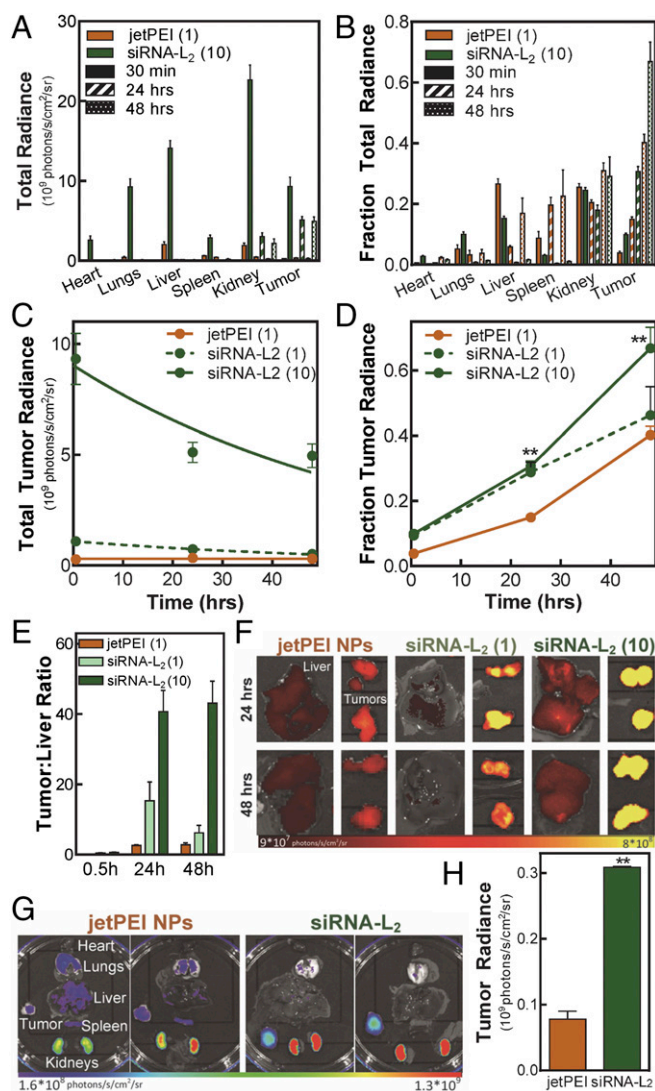| Parameter	siRNA	siRNA-L$_2$	P value
$t_{1/2}$, circulation, min	2.3 ± 0.2	13.1 ± 1.6	0.0023
AUC$_{circ, 0-\infty}$, fluor. intensity × min	5,500 ± 800	47,300 ± 6,700	0.0034
Fraction kidney radiance	0.790 ± 0.018	0.503 ± 0.014	<0.0001

AUC, area under curve.

Fig. 3. siRNA-L$_2$ achieves superior delivery to PDX and orthotopic tumors. Biodistribution was evaluated using a nontoxic dose of 1, 10 mg/kg of siRNA-L$_2$ and the MTD of 1 mg/kg jetPEI NPs. (A–F) Orthotopic model: (A) Absolute organ radiance for siRNA-L$_2$ (10 mg/kg), jet PEI NPs (1 mg/kg). (B) Fraction organ radiance for siRNA-L$_2$, jetPEI NPs. (C) Absolute tumor radiance; exponential decay fits plotted. (D) Fraction tumor radiance; **$P < 0.01$. (E) Tumor:liver ratio reveals a lower proportion in the liver for siRNA-L$_2$ in comparison with jetPEI NPs. $n = 4$, SE plotted. (F) Representative images depicting accumulation in liver, tumors. (G and H) PDX model: (G) Biodistribution and (H) plotted tumor radiance ($n = 2$) of dose-matched jetPEI NPs and siRNA-L$_2$ at 24 h. Radiance units are photons per second per square centimeter per steradian.

successful accumulation at a nonhepatic site (Fig. 3 E and F and Table 2). In contrast, jetPEI NPs displayed a tumor:liver ratio of below 3:1, a more than 15-fold decrease compared with siRNA-L$_2$ at 10 mg/kg and also lower than that observed for siRNA-L$_2$ at 1 mg/kg (which achieved a tumor:liver ratio of ~15:1).

The clear superiority of siRNA-L$_2$ in the orthotopic model motivated investigation in a more clinically relevant patient-derived xenograft (PDX) model of triple-negative breast cancer. Dose-matched siRNA-L$_2$ and in vivo jetPEI NPs at 1 mg/kg were injected i.v. and biodistribution was evaluated at 24 h. siRNA-L$_2$ attained 4.0-fold greater tumor distribution in the PDX model than jetPEI NPs (whereas there was a 2.2-fold increased tumor delivery in the dose-matched orthotopic model) at

24 h (Fig. 3 G and H and SI Appendix, Fig. S7A). Compared with the orthotopic model, achieving tumor accumulation in the PDX model was more challenging. The added challenge of PDX tumors was more detrimental for the tumor delivery with jetPEI NPs than siRNA-L$_2$. Total tumor accumulation in PDX tumors was 4.3-fold lower than orthotopic tumors for jetPEI NPs whereas it was only reduced by 2.4 fold for siRNA-L$_2$. The lower MPS accumulation of siRNA-L$_2$ relative to NPs was consistent in the PDX model, with siRNA-L$_2$ again showing a marked improvement in tumor:liver ratio (8:1 vs. 1:1) (SI Appendix, Fig. S7B).

siRNA-L$_2$ Exhibits Homogeneous Distribution and High Cellular Internalization at the Tumor Site. The small size of albumin-bound siRNA-L$_2$ is expected to increase tumor tissue penetration and homogeneity of distribution over nanoparticles. Using an in vitro tumor spheroid model, the penetration and distribution of siRNA-L$_2$ vs. jetPEI NPs throughout 3D tumor architecture was evaluated. The siRNA-L$_2$ showed homogeneous and substantial cell uptake throughout the entirety of spheroids, whereas jetPEI NPs remained localized largely around the edges of the spheroid (Fig. 4A). Unmodified siRNA showed improved penetration into the interstitial spaces compared with the jetPEI complexes, but exhibited lower overall fluorescence than siRNA-L$_2$ (SI Appendix, Fig. S8A). To complement these results, flow cytometry was used to measure uptake per cell (as quantified by mean intracellular fluorescence) in tumor spheroids that were dissociated and analyzed following siRNA formulation treatment. The cellular internalization of siRNA-L$_2$ was twofold higher than that of unmodified siRNA, evidencing an uptake benefit derived from hydrophobic modification (SI Appendix, Fig. S8B). Compared with jetPEI NPs, siRNA-L$_2$ exhibited a greater than fivefold uptake increase (Fig. 4B), with 84% of siRNA-L$_2$–treated cells positive for uptake compared with 27% of jetPEI-NP–treated cells (SI Appendix, Fig. S8 C and D).

These in vitro tumor spheroid results inspired an investigation of tumor penetration and homogeneity of internalization by cells within orthotopic breast tumors in vivo. Following i.v. injection of siRNA-L$_2$ or jetPEI NPs, cells were isolated from excised tumors and evaluated by flow cytometry for cellular internalization. Tumor cells were identified by expression of green fluorescent protein (GFP). siRNA-L$_2$ outperformed jetPEI NPs at both 30 min and 24 h, with siRNA-L$_2$ at 1 mg/kg displaying 5- and 2-fold increased uptake at respective time points and siRNA-L$_2$ at 10 mg/kg showing 45- and 20-fold increased uptake (Fig. 4C and Table 2). At 30 min, mice treated with siRNA-L$_2$ at either dose displayed uptake in more than 96% of tumor cells, whereas jetPEI-NP–treated mice showed uptake in only 60% of cells (SI Appendix, Fig. S8E). The preferential and homogeneous distribution of siRNA-L$_2$ to tumor sites and high uptake by tumor cells makes it ideally suited for cancer therapies.

siRNA-L$_2$ Elicits Sustained Silencing in an in Vivo Tumor Model. The promising tumor penetration characteristics of siRNA-L$_2$ inspired examination of its gene silencing efficacy in vivo in an orthotopic mouse tumor model. After treatment with luciferase-targeted siRNA or siRNA-L$_2$ at days 0 and 1, luminescence was evaluated over 7 d, where an increase in luminescence indicates tumor growth and successful luciferase silencing abrogates the increase in luminescent signal. siRNA-L$_2$–treated tumors exhibited significantly reduced tumor luminescence in comparison with tumors treated with unmodified luciferase-targeting siRNA or inactive, control siRNA-L$_2$ sequences (Fig. 4D and SI Appendix, Fig. S9A). Comparing to the scrambled siRNA-L$_2$ control, maximum silencing was more than 60% at day 1, with nearly 50% silencing sustained at day 7, revealing the prolonged gene silencing capacity of siRNA-L$_2$. No change in mouse body weight was observed over the course of treatment, further indicating that siRNA-L$_2$ treatment

Table 2. Key pharmacokinetic parameter comparisons of siRNA-L_2 vs. jetPEI NPs

Parameter	jetPEI NPs	siRNA-L_2 (1 mg/kg dose)	siRNA-L_2 (10 mg/kg dose)	P value$_{L_2}$ (1 mg/kg dose)	P value$_{L_2}$ (10 mg/kg dose)
AUC$_{tumor, 0.5–48\ h}$, radiance × h	1.48×10^{10}	3.61×10^{10}	2.90×10^{11}		
Liver:tumor ratio$_{24\ h,\ orthotopic}$	2.6 ± 0.2	15.4 ± 5.0	40.7 ± 5.2	0.1117	0.0007
Liver:tumor ratio$_{24\ h,\ PDX}$	1.5 ± 0.4	7.8 ± 1.8		0.1357	
Liver:tumor ratio$_{48\ h,\ orthotopic}$	2.8 ± 0.2	6.2 ± 2.6	43.1 ± 2.7	0.1739	0.0007
Fold tumor cell uptake, 30 min	7.2 ± 0.6	34.7 ± 4.7	325.2 ± 29.0	0.0001	<0.0001
Fold tumor cell uptake, 24 h	16.7 ± 1.0	31.0 ± 3.6	326.8 ± 16.0	0.0032	<0.0001

AUC, area under curve.

is well-tolerated (*SI Appendix*, Fig. S9B). Treatment with jetPEI NPs at a dose of 1 mg/kg elicited significant (∼30%) silencing at day 3, but silencing was fully abrogated by day 7 (*SI Appendix*, Fig. S9C).

As an initial proof-of-concept of activity against a therapeutically relevant gene, siRNA-L_2 that targets the negative regulator of apoptosis, myeloid leukemia cell differentiation protein (MCL-1), was synthesized. The siRNA-L_2 against MCL-1 achieved significant gene silencing in vitro at a reasonably low, 200-nM dose, and MCL-1 silencing correlated with a trend of functional increase in caspase activity (*SI Appendix*, Fig. S10).

Discussion

Simple conjugation of a hydrophobic albumin-binding diacyl lipid moiety to siRNA is a powerful delivery strategy to improve the pharmacokinetic properties of siRNA. L_2 conjugation increases circulation half-life, cellular internalization capacity, and tumor penetration and retention of siRNA while simultaneously reducing accumulation in clearance organs. These myriad benefits lead to enhanced and prolonged in vivo gene silencing in tumors, supporting siRNA-L_2 as a potential cancer therapy that can act on currently undruggable targets.

Leveraging albumin as an endogenous nanocarrier is a relatively recent but extremely promising strategy to extend the circulation persistence of therapeutics. Clinically relevant examples range from Abraxane, an albumin-based nanoparticle that encapsulates Taxol, to Levemir, a therapeutic peptide modified to associate noncovalently with endogenous albumin (35). siRNA, with its high potential medical impact but characteristically short circulation half-life, is an ideal candidate to develop with albumin as an in vivo chaperone. Inducing high-affinity binding of siRNA to albumin via modification with a lipidic moiety is a logical strategy. Previous work has shown siRNA amenable to lipid modifications, which often confer improvements in nuclease resistance and cellular internalization without impacting gene silencing (10, 14, 49, 50). Conjugation with L_2 therefore has potential benefits on enhancing molecule stability and uptake while also prompting in situ albumin binding. Notably, this binding is noncovalent and dynamic. In its physiological role as a fatty acid carrier, albumin facilitates the cellular uptake of lipids, likely through a variety of mechanisms that use receptors for both albumin and lipid domains (51, 52). Conjugation of L_2 could allow siRNA-L_2 to hijack these natural pathways. Additionally, the hydrophobic interaction of the L_2 moiety with the cellular membrane could encourage siRNA-L_2 to be internalized independent of albumin.

L_2 modification as an albumin targeting approach is desirable for achieving pharmacokinetic improvements while maintaining simplicity and safety. Despite the synthetic complexity of nanoparticle systems, siRNA-L_2 possesses a circulation half-life above that of non–cross-linked polyion nanoparticles (4, 53) and nearly equivalent to that observed in a relatively intricate cross-linked micelle system using cholesterol-modified siRNA (3). Perhaps more striking is the complete lack of toxicity observed for siRNA-L_2 at doses of 10 mg/kg, which sharply contrasts with the reported toxicity and immunogenicity of nanoparticulate carriers

and our direct evaluation of in vivo jetPEI (25, 54). siRNA-L_2 couples an improved circulation half-life with a lack of dose-limiting side effects, and therefore is anticipated to enable very broad therapeutic windows when developed against specific targets. Our demonstration of MCL-1 gene silencing and its link to caspase induction demonstrates the applicability of siRNA-L_2 to such therapeutic targets. Additionally, we expect that the efficacy of siRNA-L_2 could be further optimized through modifications to enhance in vivo stability and through identification of siRNA sequences with extremely potent silencing (55, 56).

Another associated challenge with nanoparticle delivery systems is their preferential accumulation within clearance organs, specifically the liver and spleen (8). Accumulation of synthetic and toxic/immunogenic nanoparticle components in these organs is the typical cause of dose-limiting toxicities. However, siRNA-L_2 avoids capture in the MPS organs, which is characteristic of nanoparticles, while also exhibiting a significant reduction in the
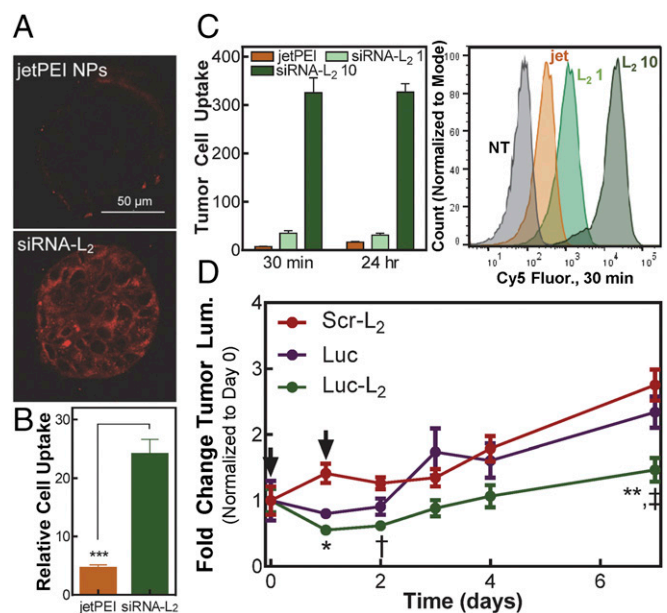

Fig. 4. siRNA-L_2 penetrates tumors and is internalized by tumor cells, resulting in sustained gene silencing in a mouse tumor model. (*A*) Representative confocal microscopy images of tumor spheroid penetration and internalization. (*B*) Cellular internalization of Cy5-labeled siRNA-L_2 or jetPEI NPs loaded with Cy5 siRNA in MCF-7 tumor spheroids, normalized to no treatment. Treatment at 100 nM, quantified by flow cytometry; $n = 3$, SE plotted, ***$P < 0.001$. (*C*) Cellular internalization in tumor cells isolated from orthotopic xenograft mouse tumors after injection of jetPEI NPs at 1 mg/kg or siRNA-L_2 at 1, 10 mg/kg, normalized to no treatment; $n = 6–8$ tumors. (*D*) Gene silencing of luciferase-targeted siRNA-L_2 compared with unmodified siRNA in an orthotopic xenograft mouse tumor model; treatment at day 0 and 1 (as indicated by arrows) at 10 mg/kg, $n = 10$. *$P < 0.05$, **$P < 0.01$: luc-L_2 vs. scr-L_2, †$P < 0.05$, ‡$P < 0.01$: luc-L_2 vs. luc. SE plotted.

rapid renal clearance associated with unmodified siRNA delivery. This is exemplified by the tumor:liver accumulation ratio of more than 40:1 achieved by siRNA-L_2. The disparity between in vivo jetPEI, with a ratio of less than 3:1, is pronounced. The lack of siRNA-L_2 retention in the liver is a key advantage over nanoparticulate delivery systems and will allow a greater percentage of the injected dose to be retained at its site of action in tumors. The lower tumor:liver ratio observed with in vivo jetPEI and nanoparticle systems in the literature is consistent with reported challenges in achieving efficient nanoparticle delivery to tumor sites; in a comprehensive analysis of nanoparticle delivery to solid tumors, the median injected dose delivered to the tumor site was 0.7% (47). It is notable that even in recent, advanced, and promising nanoparticle systems, including those that use modifications for "stealth" or targeting mechanisms, the ratio of tumor:liver accumulation is consistently close to or below 1:1 (3, 5, 57–62). The marked improvement of siRNA-L_2 in relative tumor accumulation supports its translational promise.

There is also a significant tumor penetration benefit of siRNA-L_2 due to its small size relative to nanoparticle carriers. Whereas in vivo jetPEI displays poor penetration of tumor tissue, siRNA-L_2 distributes homogeneously throughout tumor tissue and achieves consistently high uptake in tumor cells. The capacity of siRNA-L_2 to offer superior tumor penetration is particularly significant given the highly inconsistent nature of human tumor vasculature and tissue morphology which limits consistent nanoparticle distribution (47, 63). Here, we note that the PDX mouse model is less permissive to delivery than the orthotopic model. PDX models are considered more clinically relevant, as they preserve the native tissue architecture of the primary tumor through multiple in vivo passages and consistently recapitulate histopathologic and molecular characteristics, including drug responses and metastatic potential (64). The more challenging nature of the PDX model relative to the orthotopic model [which is considered more stringent than the flank model (21)] aligns with recent discussion suggesting that the permeable nature of commonly used mouse tumor models has led to an overestimation of the EPR effect (19, 20). Whereas nanocarriers like in vivo jetPEI may achieve efficacy in highly vascularized or nonsolid tumors (20), they lack the ability to diffuse throughout the bulk of tumor architecture. Faced with a more difficult delivery challenge in the PDX model, siRNA-L_2 maintains tumor accumulation better than does in vivo jetPEI. As the majority of human solid tumors contain regions of poor vascularization and display disparity in vessel permeability (20, 21), the performance of siRNA-L_2 in the PDX model suggests applicability to a much broader range of cancers. A recognition of the limitations of the EPR effect and a developing understanding of tumor heterogeneity calls for innovative solutions for systemic RNAi cancer therapies. siRNA-L_2 deviates enormously from the standard nanoparticle format, and its notable advantages should inspire further research into similar conjugate-based strategies.

In situ targeting of albumin as an endogenous carrier is a powerful strategy to enhance the bioavailability of siRNA and avoid the issues associated with synthetic nanocarriers. siRNA-L_2 surpasses conventional delivery systems in circulation persistence, safety, biodistribution profile, tumor penetration, and cellular internalization. Ultimately, siRNA-L_2 achieves sustained gene silencing in tumors in vivo, providing strong proof-of-concept for therapeutic efficacy. This work highlights the immense value of the siRNA-L_2 conjugate as a translational and potentially transformative approach to improve i.v. RNAi cancer therapies.

Materials and Methods

Materials. Amine-modified single-stranded DNA (modification at 5′ end) or RNA (modification at 3′ end) and complementary single-stranded Cy5-, unmodified DNA, or unmodified RNA was obtained from Integrated DNA Technologies (for DNA) or GE Dharmacon. The pGreenFire1-CMV plasmid was obtained from System Biosciences, and packaging plasmids pMDLg/pRRE, pRSV-Rev, and pMD2.G were purchased from Addgene. In vivo jetPEI was purchased

from VWR International. The product 1,2-distearoyl-sn-glycero-3-phosphoethanol-amine-N-[azido(polyethylene glycol)-2000] (DSPE-PEG_{2000}-azide) was purchased from Avanti Polar Lipids. NucBlue Fixed Cell ReadyProbes were purchased from Life Technologies. NAP-25 filtration columns were purchased from Fisher Scientific. RNeasy Mini Kit was purchased from Qiagen, iScript cDNA Synthesis Kit from BioRad Laboratories, and Caspase-Glo 3/7 Assay from Promega Corporation. All other reagents were purchased from Sigma-Aldrich.

Oligonucleotide-L_2 Synthesis. Single-stranded amine-modified oligo was reacted with 10-fold molar excess of dibenzocyclooctyne-PEG_4-N-hydroxy-succinimidyl ester (DBCO-PEG_4-NHS) predissolved at 25 mM in DMSO. The reaction was carried out for 18 h at room temperature at a 1 mM oligonucleotide concentration in 30% DMSO and 70% PBS with 8 mM triethylamine. The product was diluted threefold in water and filtered twice through NAP-25 columns, lyophilized, and then reacted with fivefold molar excess of DSPE-PEG_{2000}-azide for 24 h at a 0.1 mM oligonucleotide concentration in 50% methanol, 50% water. The reaction was diluted and filtered one time through a NAP-25 column and then purified with reversed-phase HPLC using a Clarity Oligo-RP column (Phenomenex) under a linear gradient from 95% water (50 mM triethylammonium acetate), 5% methanol to 100% methanol. The conjugate molecular weight was confirmed using MALDI-TOF mass spectrometry (Voyager-DE STR Workstation) using 50 mg/mL 3-hydroxypicolinic acid in 50% water, 50% acetonitrile with 5 mg/mL ammonium citrate as a matrix. The yield of the oligo-L_2 was quantified based on absorbance at 260 nm. The purified oligo-L_2 was annealed to its complementary strand to generate Cy5-modified, unmodified DNA-L_2, or siRNA-L_2. Conjugation and annealing was also confirmed via agarose gel electrophoresis.

DNA was used as a cost-effective analog for siRNA in imaging studies, and is referred to as siRNA/siRNA-L_2 in the main text and *SI Appendix* for simplicity and cohesion (except where the figure is intended to show a direct comparison between DNA and siRNA). DNA/siRNA and DNA-L_2/siRNA-L_2 exhibited degradation on similar time scales (*SI Appendix*, Fig. S3 C and D) and DNA-L_2 exhibits similar albumin binding (*SI Appendix*, Fig. S2B), validating its use as a model for siRNA-L_2.

Oligonucleotide-L_2 characterization. Critical micelle concentration (CMC) of oligo-L_2 was assessed fluorescently using Nile red, as described previously (65, 66). Briefly, different dilutions were prepared from a 1 mg/mL stock solution to obtain micelle samples ranging in concentration from 0.0001 to 1 mg/mL Then, 10 μL of a 1 mg/mL Nile red stock solution in methanol was added to 1 mL of each sample and incubated overnight in the dark at room temperature. The next day, samples were filtered with a 0.45-μm syringe filter, and Nile red fluorescence was measured in 96-well plates using a microplate reader (Tecan Infinite 500, Tecan Group Ltd.) at an excitation wavelength of 535 ± 20 nm and an emission wavelength of 612 ± 25 nm. The CMC was defined, as previously described (67), as the intersection point on the plot of the Nile red fluorescence versus the copolymer concentration.

Degradation of siRNA and siRNA-L_2 was assessed by incubation in 60% FBS for 4 h, 2 h, 1 h, 30 min, or 15 min and evaluation by agarose gel electrophoresis with comparison with a control sample in water.

Evaluation of albumin binding to oligo-L_2 in vitro. PAGE gel migration assay was used to assess binding of oligo-L_2 to BSA. Mini-Protean TGX Precast Gels of 4–20% were run in the Tetra Blotting Module (BioRad). siRNA, siRNA-L_2, DNA, and DNA-L_2 were incubated with varying amounts of BSA for 15 min. PAGE gels were stained using GelRed Nucleic Acid Stain (Biotium) according to manufacturer protocol and imaged under UV light for visualization of nucleic acid migration. Gels were subsequently stained with Coomassie blue to evaluate BSA migration.

PAGE gel migration assay was used to assess binding of oligo-L_2 to albumin in serum. siRNA or siRNA-L_2 was incubated with 9- or 13-fold molar excess BSA or 50% or 75% FBS (for approximate matching of mass of protein loaded per well). siRNA and siRNA-L_2 were imaged under UV light after poststaining with GelRed. Serum proteins were stained with Coomassie blue.

Isothermal calorimetry (ITC) experiments were performed using a TA Instruments Nano ITC. Oligo-L_2 was prepared at a concentration of 0.1 mM and BSA was dissolved at a concentration of 0.25 mM from lyophilized powder in PBS. Titration experiments were carried out at 37 °C with a 300-s initial delay, 150-rpm stirring speed, and a sample cell volume (containing DNA-L_2) of 300 μL. Each injection was 2 μL, with an injection interval of 180 s. Data were analyzed using an independent binding site model with a blank constant correction incorporated to account for heat of dilution. All data analysis was performed in Nano ITC software.

Cell Culture. Human epithelial breast cancer cells (MDA-MB-231) were cultured in DMEM (Gibco Cell Culture) supplemented with 10% FBS (Gibco) and 0.1% gentamicin (Gibco). Luciferase-expressing MDA-MB-231s were generated as previously described (5).

In Vitro Gene Silencing. MDA-MB-231 cells were treated with siRNA or siRNA-L_2 complexed with in vivo jetPEI according to the manufacturer's protocol. The siRNA was either designed against the luciferase gene (luc siRNA) or was a scrambled sequence (scr siRNA). Cells were seeded at 2,000 cells/well in 96-well black-walled plates and allowed to adhere overnight. Cells were then treated in 10% serum for 24 h at a dose of 100 or 50 nM siRNA. After 24 h, media was replaced with luciferin-containing media (150 µg/mL) before imaging with an IVIS Lumina III imaging system at 24 and 48 h.

To evaluate silencing of a therapeutically relevant gene, siRNA targeting MCL-1 was used. MCF7 cells were treated with MCL-1-targeted or a scrambled control siRNA-L_2 at 200 nM in 10% serum-containing media for 24 h. At 48 h, RNA was harvested and MCL-1 mRNA levels were evaluated using quantitative real time PCR. In parallel, caspase activity was measured at 48 h using the Caspase Glo 3/7 Assay (Promega) according to the manufacturer's protocol.

Evaluation of albumin binding to oligo-L_2 in vivo. Fluorescent (Cy-5-labeled) DNA and DNA-L_2 was injected into the tail vein of CD-1 mice (4–6-wk-old, Charles Rivers Laboratories) at 1 mg/kg. Blood was collected at 20 min postinjection, and serum was isolated. Serum from mice injected with DNA, DNA-L_2, or saline was evaluated via PAGE gel migration assay to assess binding of oligo-L_2 to albumin in vivo.

In vitro evaluation using tumor spheroids. MCF7 cells (American Type Culture Collection) were cultured in DMEM supplemented with 1% penicillin-streptomycin and 10% FBS. Three-dimensional MCF7 spheroid cultures were established as described previously (68, 69). Briefly, cells were grown to 50% confluence in 2D culture. Cells were washed twice with trypsin (0.05%, Gibco), trypsin was aspirated, and cells were incubated at 37 °C for 10–15 min. Cells were resuspended in growth medium, pipetted to generate single-cell suspensions, and counted (Bio-Rad TC20 Automated Cell Counter). Single-cell suspensions (7,500 cells per 500 µL) were seeded in eight-well chamber slides (Nunc Lab-Tek II) precoated with 10 µL growth-factor-reduced Matrigel (BD Biosciences) in growth media containing 2% growth-factor-reduced Matrigel and cultured for 5 d. The 8-well chamber slides were used for evaluation by confocal microscopy; the setup was scaled up to 12-well plates for flow cytometry and down to 96-well plates for cytotoxicity studies.

To evaluate tumor spheroid penetration by confocal microscopy, on day 5, cultures were treated with 100 nM Cy5-labeled DNA, DNA-L_2, or DNA complexed with in vivo jetPEI for 4 h in fresh growth medium. Cultures were washed once with PBS and fixed for 2 min with BD Cytofix/Cytoperm solution (BD Biosciences). After aspirating fixative and removing the plastic chamber, cultures on slides were mounted with ProLong Gold Antifade with DAPI (Molecular Probes) and secured by coverslip. Slides were stored at 4 °C before confocal imaging. Confocal imaging was performed using the Nikon C1si+ system on a Nikon Eclipse Ti-0E inverted microscopy base. The photomultiplier tube voltage, laser power, and image display settings were set for maximal signal-to-noise ratio based on control biological samples such that negative control samples lacking label had no background fluorescence and treatment samples had no saturated pixels. Image acquisition and analysis were performed using Nikon NIS Elements AR version 4.30.01.

To evaluate tumor spheroid penetration by flow cytometry, on day 5, cultures were treated as described above. Cultures were washed once with PBS and tumor cells were dissociated from Matrigel for evaluation of Cy5 fluorescence.

Blood Plasma Pharmacokinetics. Fluorescent (Cy-5-labeled) DNA and DNA-L_2 were injected into the tail vein of CD-1 mice (4–6-wk-old, Charles Rivers Laboratories) at 1 mg/kg. Before injection, the mouse ear was placed on a coverslip on the Nikon C1si+ confocal microscope system. An artery within the ear was set in focus, and after injection, images of the artery were automatically collected every 2 s for 30 min. After 30 min, animals were killed. Maximum initial fluorescence of the artery was set to a time of 0 s. Artery fluorescence was evaluated by averaging pixel intensity values contained in a circular region of interest located entirely within the vessel. Data were fit to a one-phase exponential decay model (equation below) and half-life and area under the curve were determined from these fits.

$$Fluorescence_{blood} = Fluor_0 \times e^{-kt}.$$

Biodistribution in Tumor-Bearing Mice. For the orthotopic mouse tumor model, athymic nude female mice (4–6-wk-old, Jackson Laboratory) were injected in each mammary fat pad with 1×10^6 MDA-MB-231 cells in DMEM:Matrigel (50:50). After 21 d, tumor-bearing mice were injected via the tail vein with 1 mg/kg (nucleic acid dose) of fluorescent DNA, DNA-L_2, or DNA loaded in vivo jetPEI. After 30 min, 24 h, and 48 h, animals were killed and the organs of interest (heart, lungs, liver, spleen, kidneys, and tumors) were

excised. The fluorescence intensity in the organs was quantified on an IVIS Lumina III imaging system at excitation wavelength of 620 ± 5 nm and emission wavelength of 670 ± 5 nm ($n = 3$ animals, $n = 6$ tumors). Tumor radiance data were fit to a one-phase exponential decay model (equation below), and area under the curve was determined from these fits.

$$Radiance_{tumor} = Radiance_0 \times e^{-kt}.$$

For the PDX mouse tumor model (70), the triple-negative line HCI-010 was transplanted into one inguinal mammary fat pad (surgically cleared of endogenous epithelium) of nonobese diabetic/severe combined immune-deficient (Jackson Laboratory) female mice of 3–4 wk of age (64). After ~8 wk, PDX tumors were harvested, cut into 4 mm × 2-mm pieces, serially transplanted into the cleared inguinal mammary fat pads of a new cohort of NOD-SCID female mice, and grown to a volume of 300–500 mm³. Tumor-bearing mice were injected via the tail vein with 1 mg/kg (nucleic acid dose) of fluorescent DNA-L_2 or DNA loaded in in vivo jetPEI. After 24 h, animals were killed, and the organs of interest (heart, lungs, liver, spleen, kidneys, and tumors) were excised. The fluorescence intensity in the organs was quantified on an IVIS Lumina III imaging system at excitation wavelength of 620 ± 5 nm and emission wavelength of 670 ± 5 nm ($n = 2$ animals, $n = 2$ tumors).

Acute Toxicity in Liver and Kidney. CD-1 mice were injected with siRNA-L_2 (10 mg/kg) or in vivo jetPEI-loaded siRNA (1, 2 mg/kg). After 24 h, blood was collected by cardiac puncture and then centrifuged at $2,000 \times g$ for 5 min. Then, plasma was harvested and tested by the Vanderbilt Translational Pathology Shared Resource for systemic levels of ALT, AST, BUN, and creatinine.

Tumor Distribution in Vivo After i.v. Injection. For the orthotopic tumor model, athymic nude female mice (4–6-wk-old, Jackson Laboratory) were injected in each mammary fat pad with 1×10^6 MDA-MB-231 cells in DMEM:Matrigel (50:50). After 21 d, tumor-bearing mice were injected via the tail vein with saline, 1 or 10 mg/kg fluorescent DNA-L_2, or 1 mg/kg DNA-loaded in in vivo jetPEI. Tumors were excised, and cells were isolated from each tumor. A mixture of collagenase and DNase was used to dissociate cells, and ammonium-chloride-potassium lysis buffer was used to remove red blood cells. Uptake of fluorescent DNA or DNA-L_2 was evaluated by flow cytometry ($n = 4$ animals, $n = 8$ tumors). Tumor cells were identified as the cell population expressing GFP, whereas the GFP-negative cell population corresponded to native mouse cells.

Target Gene Silencing After i.v. Injection. Athymic nude female mice (4–6-wk-old, Jackson Laboratory) were injected in each mammary fat pad with 1×10^6 MDA-MB-231 cells in DMEM:Matrigel (50:50). After tumors reached a size of 50 mm², tumor-bearing mice were injected i.p. with luciferin substrate (150 mg/kg) and imaged for bioluminescence on an IVIS Lumina III imaging system 30 min postinjection. Next, the mice were injected via the tail vein with 10 mg/kg (based on siRNA dose) luc siRNA or siRNA-L_2 or scr siRNA-L_2. Alternatively, mice were injected with 1 mg/kg in vivo jetPEI complexed with luc or scr siRNA. Mice were imaged and treated at days 0 and 1 following treatment injection and imaged for bioluminescence over time. Relative luminescence was determined by measuring the raw luminescent intensity of each tumor on each day and comparing to the initial signal at day 0 ($n = 10$ tumors per group). Mouse body weight was evaluated at each of these time points to investigate treatment toxicity.

Statistical Methods. The treatment groups were statistically compared using a one-way ANOVA test (for nonrepeated measures of more than two groups) or a two-way ANOVA (for measures repeated at multiple time points) coupled with a Tukey means comparison test. For comparison between two groups, an independent two-tailed t test was used. A P value <0.05 was deemed representative of a significant difference between groups. For all data shown, the arithmetic mean and SE are reported, and the sample size (n) is indicated.

Ethics Statement. The animal studies were conducted with adherence to the *Guide for the Care and Use of Laboratory Animals* (71). All experiments with animals were approved by Vanderbilt University's Institutional Animal Care and Use Committee.

1. Soutschek J, et al. (2004) Therapeutic silencing of an endogenous gene by systemic administration of modified siRNAs. *Nature* 432:173–178.
2. Davis ME, et al. (2010) Evidence of RNAi in humans from systemically administered siRNA via targeted nanoparticles. *Nature* 464:1067–1070.
3. Oe Y, et al. (2014) Actively-targeted polyion complex micelles stabilized by cholesterol and disulfide cross-linking for systemic delivery of siRNA to solid tumors. *Biomaterials* 35:7887–7895.
4. Miteva M, et al. (2015) Tuning PEGylation of mixed micelles to overcome intracellular and systemic siRNA delivery barriers. *Biomaterials* 38:97–107.
5. Sarett S (2016) Hydrophobic interactions between polymeric carrier and palmitic acid-conjugated siRNA improve pegylated polyplex stability and enhance in vivo pharmacokinetics and tumor gene silencing. *Biomaterials* 97:122–32.
6. Lv H, Zhang S, Wang B, Cui S, Yan J (2006) Toxicity of cationic lipids and cationic polymers in gene delivery. *J Controlled Release* 114:100–109.
7. Akhtar S, Benter I (2007) Toxicogenomics of non-viral drug delivery systems for RNAi: Potential impact on siRNA-mediated gene silencing activity and specificity. *Adv Drug Deliv Rev* 59:164–182.
8. Owens DE, 3rd, Peppas NA (2006) Opsonization, biodistribution, and pharmacokinetics of polymeric nanoparticles. *Int J Pharm* 307:93–102.
9. Østergaard ME, et al. (2015) Efficient synthesis and biological evaluation of 5′-galnac conjugated antisense oligonucleotides. *Bioconjug Chem* 26:1451–1455.
10. Kubo T, Takei Y, Mihara K, Yanagihara K, Seyama T (2012) Amino-modified and lipid-conjugated dicer-substrate siRNA enhances RNAi efficacy. *Bioconjug Chem* 23:164–173.
11. Lorenz C, Hadwiger P, John M, Vornlocher HP, Unverzagt C (2004) Steroid and lipid conjugates of siRNAs to enhance cellular uptake and gene silencing in liver cells. *Bioorg Med Chem Lett* 14:4975–4977.
12. Dobrovolskaia MAAP, Aggarwal P, Hall JB, McNeil SE (2008) Preclinical studies to understand nanoparticle interaction with the immune system and its potential effects on nanoparticle biodistribution. *Mol Pharm* 5:487–495.
13. Shi JXZ, Kamaly N, Farokhzad OC (2011) Self-assembled targeted nanoparticles: Evolution of technologies and bench to bedside transition. *Acc Chem Res* 44:1123–1134.
14. Wolfrum C, et al. (2007) Mechanisms and optimization of in vivo delivery of lipophilic siRNAs. *Nat Biotechnol* 25:1149–1157.
15. Matsuda S, et al. (2015) siRNA conjugates carrying sequentially assembled trivalent N-acetylgalactosamine linked through nucleosides elicit robust gene silencing in vivo in hepatocytes. *ACS Chem Biol* 10:1181–1187.
16. Rajeev KG, et al. (2015) Hepatocyte-specific delivery of siRNAs conjugated to novel non-nucleosidic trivalent N-acetylgalactosamine elicits robust gene silencing in vivo. *ChemBioChem* 16:903–908.
17. Commisso C, et al. (2013) Macropinocytosis of protein is an amino acid supply route in Ras-transformed cells. *Nature* 497:633–637.
18. Kamphorst JJ, et al. (2015) Human pancreatic cancer tumors are nutrient poor and tumor cells actively scavenge extracellular protein. *Cancer Res* 75:544–553.
19. Danhier F (2016) To exploit the tumor microenvironment: Since the EPR effect fails in the clinic, what is the future of nanomedicine? *J Control Release* 244:108–121.
20. Nichols JW, Bae YH (2014) EPR: Evidence and fallacy. *J Control Release* 190:451–464.
21. Prabhakar U, et al. (2013) Challenges and key considerations of the enhanced permeability and retention effect for nanomedicine drug delivery in oncology. *Cancer Res* 73:2412–2417.
22. Jain RK, Stylianopoulos T (2010) Delivering nanomedicine to solid tumors. *Nat Rev Clin Oncol* 7:653–664.
23. Bae YH, Park K (2011) Targeted drug delivery to tumors: Myths, reality and possibility. *J Control Release* 153:198–205.
24. Eliasof S, et al. (2013) Correlating preclinical animal studies and human clinical trials of a multifunctional, polymeric nanoparticle. *Proc Natl Acad Sci USA* 110:15127–15132.
25. Zuckerman JE, et al. (2014) Correlating animal and human phase Ia/Ib clinical data with CALAA-01, a targeted, polymer-based nanoparticle containing siRNA. *Proc Natl Acad Sci USA* 111:11449–11454.
26. Kai MP, et al. (2016) Tumor presence induces global immune changes and enhances nanoparticle clearance. *ACS Nano* 10:861–870.
27. Dong Y, et al. (2014) Lipopeptide nanoparticles for potent and selective siRNA delivery in rodents and nonhuman primates. *Proc Natl Acad Sci USA* 111:3955–3960.
28. Martin JD, Fukumura D, Duda DG, Boucher Y, Jain RK (2016) Reengineering the tumor microenvironment to alleviate hypoxia and overcome cancer heterogeneity. *Cold Spring Harb Perspect Med* 6:a027094.
29. Reuter KG, et al. (2015) Targeted print hydrogels: The role of nanoparticle size and ligand density on cell association, biodistribution, and tumor accumulation. *Nano Lett* 15:6371–6378.
30. Tong R, Langer R (2015) Nanomedicines targeting the tumor microenvironment. *Cancer J* 21:314–321.
31. Clark AJWD, et al. (2016) CRLX101 nanoparticles localize in human tumors and not in adjacent, nonneoplastic tissue after intravenous dosing. *Proc Natl Acad Sci USA* 113:3850–3854.
32. Hammond PT (2016) Shooting for the moon: Nanoscale approaches to cancer. *ACS Nano* 10:1711–1713.
33. Wong C, et al. (2011) Multistage nanoparticle delivery system for deep penetration into tumor tissue. *Proc Natl Acad Sci USA* 108:2426–2431.
34. Ernsting MJ, Murakami M, Roy A, Li SD (2013) Factors controlling the pharmacokinetics, biodistribution and intratumoral penetration of nanoparticles. *J Control Release* 172:782–794.
35. Kratz F (2008) Albumin as a drug carrier: Design of prodrugs, drug conjugates and nanoparticles. *J Control Release* 132:171–183.
36. Qin S, et al. (2014) A physiological perspective on the use of imaging to assess the in vivo delivery of therapeutics. *Ann Biomed Eng* 42:280–298.
37. Neumann E, et al. (2010) Native albumin for targeted drug delivery. *Expert Opin Drug Deliv* 7:915–925.
38. Cohen JLCJ, et al. (1998) Improved left ventricular endocardial border delineation and opacification with OPTISON (FS069), a new echocardiographic contrast agent. Results of a phase III Multicenter Trial. *J Am Coll Cardiol* 32:746–752.
39. Kuwahara H, et al. (2011) Efficient in vivo delivery of siRNA into brain capillary endothelial cells along with endogenous lipoprotein. *Mol Ther* 19:2213–2221.
40. Nakayama T, et al. (2012) Harnessing a physiologic mechanism for siRNA delivery with mimetic lipoprotein particles. *Mol Ther* 20:1582–1589.
41. Uno Y, et al. (2011) High-density lipoprotein facilitates in vivo delivery of α-tocopherol-conjugated short-interfering RNA to the brain. *Hum Gene Ther* 22:711–719.
42. Bienk K, et al. (2016) An albumin-mediated cholesterol design-based strategy for tuning sirna pharmacokinetics and gene silencing. *J Control Release* 232:143–151.
43. Lau S, et al. (2012) Enhanced extravasation, stability and in vivo cardiac gene silencing via in situ siRNA-albumin conjugation. *Mol Pharm* 9:71–80.
44. Liu H, et al. (2014) Structure-based programming of lymph-node targeting in molecular vaccines. *Nature* 507:519–522.
45. Levy OE, et al. (2014) Novel exenatide analogs with peptidic albumin binding domains: Potent anti-diabetic agents with extended duration of action. *PLoS One* 9:e87704.
46. Chen H, et al. (2016) Chemical conjugation of evans blue derivative: A strategy to develop long-acting therapeutics through albumin binding. *Theranostics* 6:243–253.
47. Wilhelm S, et al. (2016) Analysis of nanoparticle delivery to tumours. *Nat Rev Mater* 1:16014.
48. Sidi AA, et al. (2008) Phase I/II marker lesion study of intravesical BC-819 DNA plasmid in H19 over expressing superficial bladder cancer refractory to bacillus Calmette-Guerin. *J Urol* 180:2379–2383.
49. Sarett SM, Kilchrist KV, Miteva M, Duvall CL (2015) Conjugation of palmitic acid improves potency and longevity of siRNA delivered via endosomolytic polymer nanoparticles. *J Biomed Mat Res A* 103:3107–3116.
50. Ambardekar VV, et al. (2011) The modification of siRNA with 3′ cholesterol to increase nuclease protection and suppression of native mRNA by select siRNA polyplexes. *Biomaterials* 32:1404–1411.
51. McArthur MJAB, et al. (1999) Cellular uptake and intracellular trafficking of long chain fatty acids. *J Lipid Res* 40:1371–1383.
52. Trigatti BLGG, Gerber GE (1995) A direct role for serum albumin in the cellular uptake of long-chain fatty acids. *Biochem J* 308:155–159.
53. Zuckerman JE, Choi CH, Han H, Davis ME (2012) Polycation-siRNA nanoparticles can disassemble at the kidney glomerular basement membrane. *Proc Natl Acad Sci USA* 109:3137–3142.
54. Ozpolat B, Sood AK, Lopez-Berestein G (2014) Liposomal siRNA nanocarriers for cancer therapy. *Adv Drug Deliv Rev* 66:110–116.
55. Behlke MA (2008) Chemical modification of siRNAs for in vivo use. *Oligonucleotides* 18:305–319.
56. Rettig GR, Behlke MA (2012) Progress toward in vivo use of siRNAs-II. *Mol Ther* 20:483–512.
57. Park J, Park J, Pei Y, Xu J, Yeo Y (2016) Pharmacokinetics and biodistribution of recently-developed siRNA nanomedicines. *Adv Drug Deliv Rev* 104:93–109.
58. Chen Y, et al. (2014) Highly effective inhibition of lung cancer growth and metastasis by systemic delivery of siRNA via multimodal mesoporous silica-based nanocarrier. *Biomaterials* 35:10058–10069.
59. Lee MS, et al. (2014) Target-specific delivery of sirna by stabilized calcium phosphate nanoparticles using dopa-hyaluronic acid conjugate. *J Control Release* 192:122–130.
60. Choi KYSO, et al. (2014) Versatile RNA interference nanoplatform for systemic delivery of RNAs. *ACS Nano* 8:4559–4570.
61. Zhu X, et al. (2015) Long-circulating siRNA nanoparticles for validating Prohibitin1-targeted non-small cell lung cancer treatment. *Proc Natl Acad Sci USA* 112:7779–7784.
62. Bartlett DW, Su H, Hildebrandt IJ, Weber WA, Davis ME (2007) Impact of tumor-specific targeting on the biodistribution and efficacy of siRNA nanoparticles measured by multimodality in vivo imaging. *Proc Natl Acad Sci USA* 104:15549–15554.
63. Nagy JA, et al. (2006) Permeability properties of tumor surrogate blood vessels induced by VEGF-A. *Lab Invest* 86:767–780.
64. DeRose YS, et al. (2013) Patient-derived models of human breast cancer: Protocols for in vitro and in vivo applications in tumor biology and translational medicine. *Curr Protoc Pharmacol*, 10.1002/0471141755.ph1423s60.
65. Gupta MK, Meyer TA, Nelson CE, Duvall CL (2012) Poly(PS-b-DMA) micelles for reactive oxygen species triggered drug release. *J Control Release* 162:591–598.
66. Fowler SDGP (1985) Application of nile red, a fluorescent hydrophobic probe, for the detection of neutral lipid deposits in tissue sections. *J Histochem Cytochem* 33:833–836.
67. Coutinho PJGCE, Ceu Rei M (2002) Real Oliveira MECD. Nile red and DCM fluorescence anisotropy studies in c12e7/dppc mixed systems. *J Phys Chem B* 106:12841–12846.
68. Debnath J, Muthuswamy SK, Brugge JS (2003) Morphogenesis and oncogenesis of MCF-10A mammary epithelial acini grown in three-dimensional basement membrane cultures. *Methods* 30:256–268.
69. Brantley-Sieders DM, et al. (2011) Angiocrine factors modulate tumor proliferation and motility through EphA2 repression of Slit2 tumor suppressor function in endothelium. *Cancer Res* 71:976–987.
70. DeRose YS, et al. (2011) Tumor grafts derived from women with breast cancer authentically reflect tumor pathology, growth, metastasis and disease outcomes. *Nat Med* 17:1514–1520.
71. National Research Council (2011) *Guide for the Care and Use of Laboratory Animals* (National Academies Press, Washington, DC), 8th Ed.

Sarett et al.